# Sheffield Hallam University

# Thermoelectric performance of tellurium-reduced quaternary p-type lead-chalcogenide composites

AMINORROAYA YAMINI, Sima <http://orcid.org/0000-0002-2312-8272>, WANG, H., GIBBS, Z.M., PEI, Y., MITCHELL, D.R.G., DOU, S.X. and SNYDER, G.J.

## Published version

## Copyright and re-use policy

# Thermoelectric Properties and Microstructure Studies of Spinodally Decomposed PbTe$_{0.38}$S$_{0.62}$ Alloy

Sima Aminorroaya[1,*], Alex Zevalkink Williams[2], Darren Attard[1], G. Shi Xue Dou[1], and G. Jeffrey Snyder[2]

[1]Institute for Superconducting and Electronic Materials (ISEM), Innovation Campus,
University of Wollongong, NSW 2519, Australia
[2]Materials Science, California Institute of Technology, Pasadena, CA 91125, USA

## ABSTRACT

PbTe is a premiere mid-range temperature thermoelectric material and recent studies have proven nanostructuring as an effective approach to reduce thermal conductivity of alloys. Whereas, little attention has been given to long-term thermal stability of secondary phases and microstructural evolution. Interestingly, replacing Te with S in PbTe provides an opportunity to form nanostructures in the bulk material through spinodal decomposition, which appears in binary phase diagrams of the PbTe–PbS system. Herein, the critical composition of PbTe$_{0.38}$S$_{0.62}$ alloy is fabricated to *n*-type by chlorine doping. Thermoelectric transport properties of the alloy are investigated in the 300–850 K temperature range and the maximum *zT* achieved at 800 K is 0.75 with a predicted *zT* $\sim$ 0.85 at 750 K from single parabolic band model. The microstructure of the sintered samples was studied by FEG-SEM for both the as sintered and post transport properties measurement. The experimental results are compared with estimates from the parallel and series models for heterogeneous composites of single phase PbTe and PbS. The Seebeck coefficient is in agreement with the models predictions, but the resistivity is higher and the thermal conductivity is much lower than predicted values. We propose that this is attributed to the phonon and electron scattering on solute atoms in solid solutions and at interfaces.

**KEYWORDS:**

## 1. INTRODUCTION

Solid-state thermoelectric convertors, using thermoelectric materials, are considered promising candidates for complementary clean and renewable energy sources. Although a feasible thermoelectric generator for primary power generation requires thermoelectric materials with *zT* above 1.5 at an 800 °C operation temperature,[1] the small size, rapid response and robustness of thermoelectric generators have made them competing candidates for other applications.[2] The efficiency of thermoelectric materials is determined by the dimensionless figure of merit, $zT = S^2 T\sigma/(\kappa_E + \kappa_L)$, which is a function of lattice thermal conductivity ($\kappa_L$), electronic thermal conductivity ($\kappa_E$), the Seebeck coefficient ($S$), electrical conductivity ($\sigma$), and absolute temperature. Nanostructured thermoelectric materials such as thin-film superlattices and nanowires, exhibit higher *zT* compared to their bulk counterparts, due to the reduction in thermal conductivity by phonon scattering mechanisms

and/or an increase in Seebeck coefficient ($S$) from quantum effects.[3,4] However, they cannot be used for high volume applications, so nanostructuring should be utilized in bulk materials.

A large number of recent studies[5–10] have focused on the so-called mid-range temperature (600–900 K) thermoelectric materials and specifically PbTe, where the majority of broad-based applications benefit. Recent studies[7–9,11,12] have improved PbTe thermoelectric performance significantly through tuning the electronic structure and/or nanostructuring of bulk materials. However, Te is rare in the Earth's crust, used in other applications[13] and is expensive hence the focus in the latest studies[14–17] trying to replace Te with Se or S.[18,19] Sulphur is amongst the 16 most abundant elements in the Earth's crust[13] and replacing Te, partially with S also provides a fascinating opportunity to form fine lamellar microstructure through spinodal decomposition, which appears in binary phase diagrams of the PbTe–PbS system. Lamellar patterns resembling a eutectic structure have been demonstrated for several thermoelectric materials[17,20–22] and thermal conductivity reduction has been reported, specifically for PbTe–PbS system,[14,17,23]

**ARTICLE**

where the reduction in thermal conductivity was essentially attributed to an increase in phonon scattering at the interfaces. However, neither of the selected compounds in PbTe–PbS system exhibits the critical composition, where the composition passes through the top of the miscibility gap (the critical point). Moreover, long-term stability at high temperature and microstructural evolution is not discussed. Recent study.[24] on spinodally decomposed PbTe–GeTe has shown that the figure of merit at room temperature is improved when the solid solution is slightly decomposed and the improvement disappears upon the coarsening of the nanostructure.

In the present work, lamellar PbTe–PbS structure is obtained in the critical composition of PbTe$_{0.62}$S$_{0.38}$ alloy. In order to avoid deterioration of transport properties by coarsening of the microstructure through experiments, the structure was kept at the annealing temperature, allowing for slow structural relaxation and coarsening, to approach the equilibrium state. The electronic transport properties were measured over the temperature range of 300–850 K and compared with composites of individual compounds. The microstructure is studied carefully in the as sintered sample and post transport properties measurements. The Single Parabolic Band (SPB) model was adopted to predict the optimised figure of merit.

## 2. EXPERIMENTAL DETAILS

### 2.1. Synthesis

Polycrystalline samples of PbS and PbTe were prepared by appropriately mixing high purity Pb (99.999%), Te (99.9999%) and dried S (99.9%) in vacuum sealed quartz ampoules at a residual pressure of $\sim 10^{-4}$ torr, and reacted in a high temperature furnace to produce high purity PbTe and PbS starting materials. The final Polycrystalline PbTe$_{0.62}$S$_{0.38}$ samples were synthesized by mixing appropriate stoichiometric quantity of high purity PbS, PbTe and 0.1 mol% PbCl$_2$ as a dopant, with a total mass of 10 g, sealed in carbon-coated quartz tubes under vacuum, then heated to 1323 K at $\sim$100 K/h. After soaking at 1323 K for approximately 6 hours, the sample was cooled to room temperature followed by annealing at 773 K for 48 h. The resulting ingot was hand ground to powder and sintered at 773 K for 1 h in a 12 mm diameter graphite mould, at an axial pressure of 40 MPa under argon atmosphere by induction hot pressing.

### 2.2. Resistivity and Hall Measurements

Samples were loaded onto a heated BN substrate and four probes were attached to the edge of the sample. The sample was placed in vacuum with a magnetic field (up to $\pm 2$ T) perpendicular to its surface. The resistivity $\rho$ and Hall coefficient $R_H$ (along the in-plane direction) were measured using the Van de Pauw method. The Hall carrier density ($n_H = 1/e \cdot r_H$) and mobility ($\mu = r_H/\rho$) were then calculated based on the measured $R_H$.

### 2.3. Seebeck Coefficient Measurements

The Seebeck coefficients were obtained along the sample's cross-plane direction. The samples were placed in contact with a heater on each surface in a vacuum chamber. Two Nb-Chromel thermocouples were also pressed against the two surfaces of the sample by spring force. The heaters were programmed to provide a temperature difference oscillation between $\pm 7$ °C whilst maintaining a set average temperature. The thermoelectric voltage and temperature on each surface were recorded, with the slope giving the Seebeck coefficient at the average temperature.

### 2.4. Thermal Conductivity Measurements

The thermal conductivity $\kappa$ is calculated from $\kappa = \rho D_T C_p$. The laser flash method (Netzsch LFA457) was used to measure Thermal diffusivity $D_T$, density, $\rho$, was calculated using the measured weight and dimensions, and the specific heat capacity, $C_p$, was estimated by:

$$C_p \ (k_B \text{ per atom}) = 3.07 + 4.7 \times 10^{-4} \times (T/K - 300)$$

The combined uncertainty for all measurements involved in $zT$ determination is $\sim 20\%$.

### 2.5. Microstructure Analysis

The crystallographic structure and composition were characterized by X-ray Diffraction (XRD) using a PANalytical X'Pert Pro X-ray diffractometer with Cu K$_\alpha$ radiation ($\lambda = 1.544$ Å, 40 kV, 30 mA). The microstructures were analysed by a a JEOL JSM-7500FA Field Emission Gun-Scanning Electron Microscopy (FEG-SEM), equipped with a Bruker X-Flash 4010 Energy Dispersive Spectroscopy (EDS) detector.

## 3. RESULTS AND DISCUSSION

### 3.1. Microstructure

According to the quasi-binary phase diagram of PbS–PbTe,[25] shown in Figure 1, there is unlimited solubility of PbS and PbTe phases in both liquid and solid states at temperatures above 1070 K. At lower temperatures, S-rich
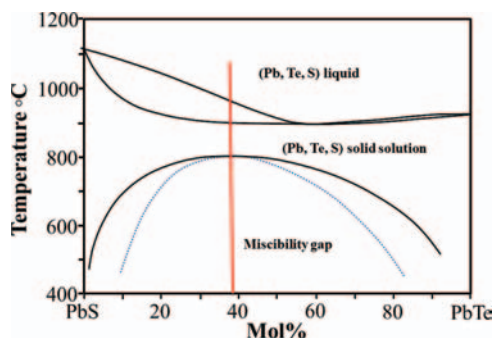


**Fig. 1.** Quasi-binary PbS–PbTe phase diagram, data points are extracted from Ref. [25]. The coordinates of the critical point are 1070 K and 38 mole% PbTe.
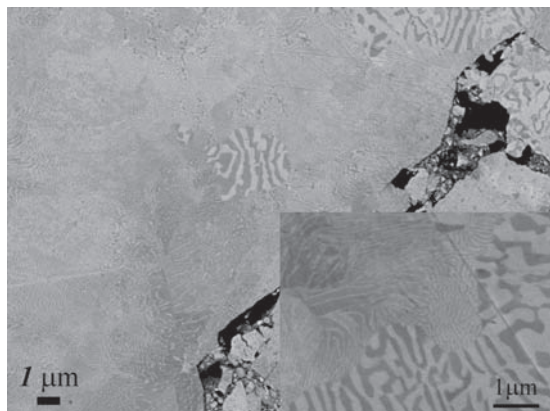
**Fig. 2.** Back scattered SEM image of the annealed sample sintered at 773 K for an hour prior to transport properties measurements. The bright phase is corresponding to PbTe phase and dark phase represents PbS phase.

and Te-rich NaCl structure PbS(Te) and PbTe(S) form. The critical composition of PbTe$_{0.62}$S$_{0.38}$ passes through the top of the miscibility resulting in an entirely lamellar pattern of PbTe–PbS alloy as represented in Figure 2. The lamellar patterns are divided into two categories of eutectoid transformation and discontinuous precipitation.[24] In the eutectoid transformation, the parent phase decomposes into two distinctive crystallographic phases, while discontinuous precipitation involves the formation of a new phase in a solute depleted matrix. In order to distinguish the phases and measure the ratio of individual compounds, the X-ray diffraction pattern of the composite is indexed and refined using Rietveld analysis in Figure 3. The XRD pattern shows two distinct phases of PbTe and PbS with 49.5 wt% PbTe in the composite, which is higher than the theoretical value of 46 wt% for the nominal composition. The distinct composition of phases regardless of the shape and size of each phase in the lamellar structure, confirms the eutectoid-like transformation which is characteristic of discontinuous reactions.[24] The lattice parameter from the pattern was calculated to be $a = 5.95$ Å and $a = 6.42$ Å for PbS and PbTe respectively compared to $a = 5.93$ Å and $a = 6.46$ Å for pure PbS and PbTe. It is
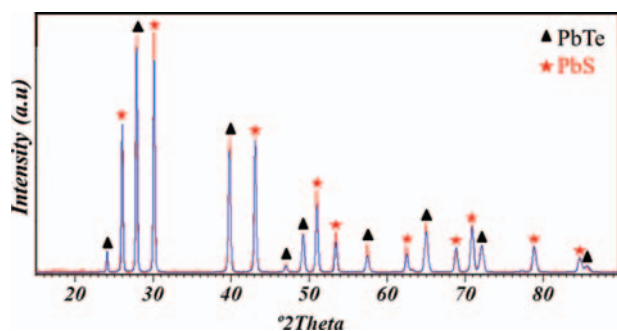


**Fig. 3.** Room temperature powder X-ray diffraction pattern for PbTe and PbS (red lines) from 20° to 90°, together with the fit of the model to intensities (blue lines).

shown that the PbS unit cell volume has been increased due to the substitution of larger Te atoms for S in PbS(Te), and the PbTe unit cell volume has been reduced by the substitution of S for Te in PbTe(S). Therefore the phase ratio is deviated from pure PbTe and PbS phase, which describes the variation of phase ratios from nominated composition.

Nanostructures in materials can be created by nano-precipitation in the matrix, nanograins (introducing grain boundaries) and nanocomposites. Spinodally decomposed alloys fall into the nanocomposites category. Their complicated topology, created by simultaneously movement of grain boundaries causes each phase to be surrounded by other one. Due to the nature of spinodal decomposition, the products remain in a non-equilibrium condition in terms of the composition. The small interlamellar spacing imposes a considerable amount of phase boundaries to the system. This in turn provides a considerable amount of free energy for further microstructural evolution. The slow cooling rate followed by annealing at 773 K leads to significant coarsening of the structure. Figure 2 shows that the interlamellar spacing is varied in different grains. It might be attributed to the discontinuous coarsening of lamellar structure at grains with different size and crystallographic orientation.

### 3.2. Transport Properties

The electronic transport properties of the spinodally decomposed compound are shown in Figure 4 for the temperature range of 300–850 K. PbCl$_2$ has been used as an $n$-type dopant. Each chlorine atom is expected to donate one extra electron to the compound that offers approximately $3 \times 10^{19}$ cm$^{-3}$ carriers. The Hall carrier concentration of the sample at room temperature is measured equal to $2.8 \times 10^{19}$ cm$^{-3}$. The difference is within the experimental error.

The lattice thermal conductivity is calculated by subtracting the electronic thermal conductivity using the Widemann-Franz relationship $\kappa_e = LT/\rho$. Where $\rho$ is the resistivity, and $L$ is the Lorenz number estimated as a function of temperature, through fitting the reduced chemical potential $\eta$ obtained from the Seebeck coefficient, $S$, as expressed in Eq. (1). The acoustic phonon scattering and SPB model[26] was assumed for this calculation.

$$S = \frac{k}{e}\left(\frac{2F_1(\eta)}{F_0(\eta)} - \eta\right) \quad (1)$$

The $\eta$ values that fit the temperature dependant $S$ is used to calculate $L$ through Eq. (2):

$$L = \left(\frac{k}{e}\right)\frac{3F_0(\eta)F_2(\eta) - 4F_1(\eta)^2}{F_0(\eta)^2} \quad (2)$$

The Lorenz number versus temperature is shown in Figure 4(c). By temperature increment, the Lorenz number decreases as $\eta$ is decreasing. At high temperatures,
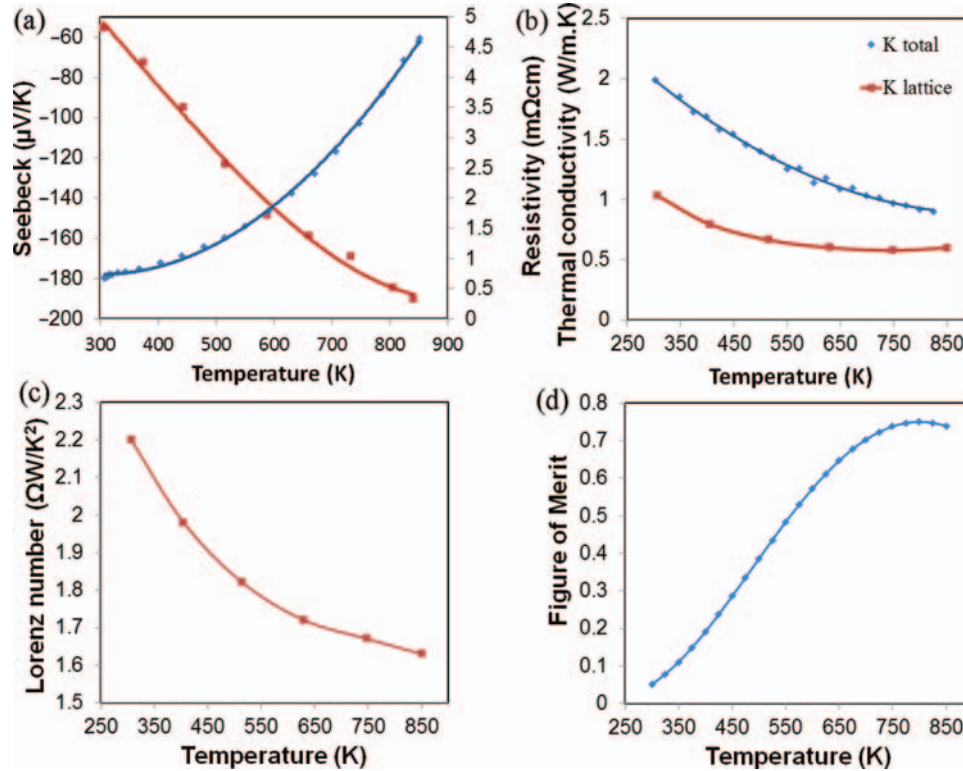
**Fig. 4.** Thermoelectric properties of PbTe$_{0.62}$S$_{0.38}$ alloy, doped with 0.1 mol% PbCl$_2$. (a) Electrical resistivity and seebeck coefficient as a function of sample temperature, (b) total thermal conductivity and lattice thermal conductivity as a function of sample temperature, (c) Lorenz number as a function of sample temperature, (d) figure of merit ($zT$) as a function of sample temperature.

the single-band model can fail if the band gap is small enough to allow both holes and electrons to be present and bipolar diffusion taken place. If this happens, the Lorenz number calculated in this manner shows an upturn at high temperatures.[26] This event is not observed for the current sample, which indicates that bipolar diffusion only has a minor effect on the transport properties for this doping level and temperature range.

The thermoelectric figure of merit $zT$ is shown in Figure 4(d). The maximum value is found to be $\sim 0.75$ at 800 K. In order to compare the transport properties of the spinodally decomposed alloy with pure PbTe and PbS, the experimental data of pure $n$-type PbTe and PbS with similar carrier concentration was used from literature[14, 27] and compared with estimations from the parallel and series models[28] in Figure 5 at 300 K and 700 K. These models are used to bracket the properties of heterogeneous materials at any microscopic configurations between upper and lower bounds respectively. The equations for the models are summarized in Table I. Figure 5(a) shows the Seebeck coefficient of the sample lies between parallel and series models as expected while Figure 5(b) illustrates that the electrical resistivity of the sample is slightly higher than estimated values from the upper bound model. It is worth noting that solid solution in single phase thermoelectric materials is traditionally used to reduce thermal conductivity through scattering of phonons. However, electrical

conductivity is decreased as well due to scattering of carriers. The parallel and series models describe the properties of hybrid materials where the chemical composition and consequently physical properties of each phase is equal to the starting individual compounds. However, the PbTe(S) and PbS(Te) phases which are spinodally decomposed are solid solutions of Te-rich and S-rich PbS–PbTe respectively. Therefore, at the same doping level it is expected that the electrical resistivity of either compounds would be higher than pure phases due to scattering occurred in solid solution phases. Consequently, it is anticipated that the current sample achieved higher electrical resistivity values than the estimated model values.

Figure 5(c) shows that the thermal conductivity of the PbTe$_{0.62}$S$_{0.38}$ composite is significantly lower than the bounds derived from the parallel and series models. These results denote that phonon scattering has occurred due to disorder rising from solute atoms in solid solution as discussed above, and also through interfaces of the lamellar pattern. Although the interlamellar spacing has been increased by equilibration at high temperatures, compared to previous studies,[17] phonon scattering by boundaries and interfaces played a significant role in the thermal conductivity reduction.

Gorsse et al.[24] investigated the effect of aging on room temperature transport properties of spinodally decomposed PbTe-GeTe alloy and showed that by annealing
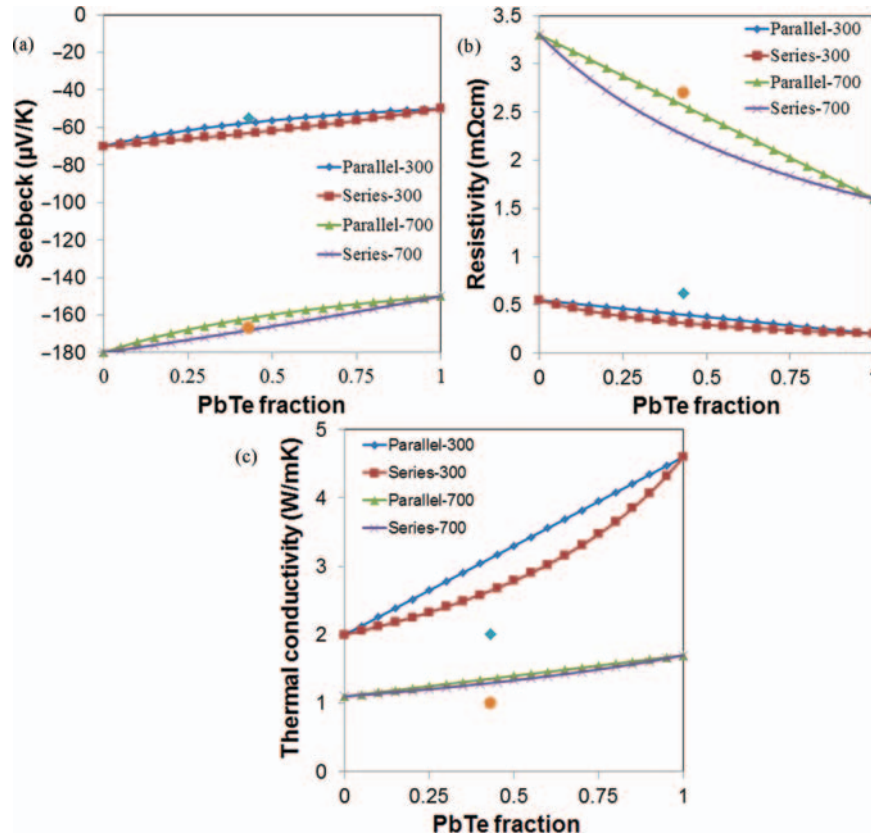
**Fig. 5.** (a) Seebeck coefficient ($S$) versus PbTe volume fraction, (b) electrical resistivity ($1/\sigma$) versus PbTe volume fraction and (c) thermal conductivity versus PbTe volume fraction of PbTe$_{0.62}$S$_{0.38}$ alloy estimated from parallel and series models at 300 and 700 K.

the quenched sample at 773 K from 1 to 1000 minutes ($\sim 17$ hours), the transport properties are changing by evolution of the microstructure. However there is only a slight difference between the measured transport properties, for samples aged longer than 100 minutes. In the present study, annealing at 773 K for 48 hours is considered to obtainequilibrium, and the transport property measurements were performed on a single sample. Therefore several heating/cooling cycles within the 300 K to 850 K temperature range were applied to the sample within a few days of measurements. The SEM image of the sample after measurement is illustrated in Figure 6. Comparing the lamellar pattern with the as sintered sample in Figure 2 clearly demonstrates the coarsening of the lamellar structure. The large fraction of interfaces and partial

dissolution of both phases by increasing the temperature, and re-precipitation during cooling accelerate the coarsening of the lamellar patterns.

### 3.3. Modelling

The Single parabolic band model was employed to estimate the optimized thermoelectric efficiency in this alloy.[26]

**Table I.** Analytical models for effective properties of two phase materials.[28]

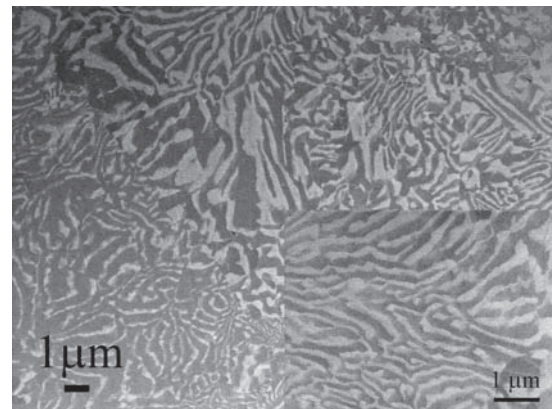| | Thermal and electrical conductivity ($\lambda$) | Seebeck coefficient ($S$) |
|---|---|---|
| Parallel model (upper limit) | $\lambda = \lambda_1 f_1 + \lambda_2(1-f_1)$ | $S = \dfrac{S_1\sigma_1 f_1 + S_2\sigma_2(1-f_1)}{\sigma_1 f_1 + \sigma_2(1-f_1)}$ |
| Series model (lower limit) | $\lambda = \dfrac{\lambda_1\lambda_2}{\lambda_1(1-f_1)+\lambda_2 f_1}$ | $S = \dfrac{S_1\kappa_2 f_1 + S_2\kappa_1(1-f_1)}{\kappa_2 f_1 + \kappa_1(1-f_1)}$ |



**Fig. 6.** Back scattered SEM image of the sintered composite after transport property measurements where the sample has been through several cycles of heat treating within the 300 K and 850 K temperature range. PbTe and PbS correspond to the bright and dark phases respectively.

ARTICLE

The model employs the Fermi integral $F_j$:

$$F_j(\eta) = \int_0^\infty f\varepsilon^j d\varepsilon = \int_0^\infty \frac{\varepsilon^j d\varepsilon}{1 + \exp(\varepsilon - \eta)} \qquad (3)$$

Where $\eta$ is the reduced chemical potential and the reduced Fermi level is calculated from Eq. (1). The effective mass ($m^*$) estimated from Eq. (4) using $\eta$, temperature and carrier concentration ($n$), Where $h$ is Planck's constant:

$$n = 4\pi \left( \frac{2m^*kT}{h^2} \right)^{3/2} F_{1/2} \qquad (4)$$

Where the Hall coefficient for acoustic phonon scattering is given by:

$$r_H = \frac{3}{2} F_{1/2} \frac{F_{-1/2}}{2F_0^2} \qquad (5)$$

The mobility parameter, $\mu_0$, should be estimated at the temperature of interest. The Hall mobility $\mu_H = (\rho n_H e)^{-1}$ and Eq. (6) are employed to estimate $\mu_0$:

$$\mu_H = \mu_0 \frac{F_{-1/2}}{2F_0^2} \qquad (6)$$

The Lorenz number and lattice thermal conductivity were calculated as discussed in the previous section. In order to calculate a theoretical $zT$ versus carrier concentration, parameters $m^*$, $\mu_0$ and $\kappa_L$ at the temperature of interest were used to calculate the $\beta$ parameter and function $\psi$:

$$\beta = \frac{\mu_0 (m^*/m_e)^{3/2} T^{5/2}}{\kappa_L} \qquad (7)$$

$$\psi = \frac{8\pi e}{3} \left( \frac{2m_e k}{h^2} \right)^{3/2} F_0 \qquad (8)$$
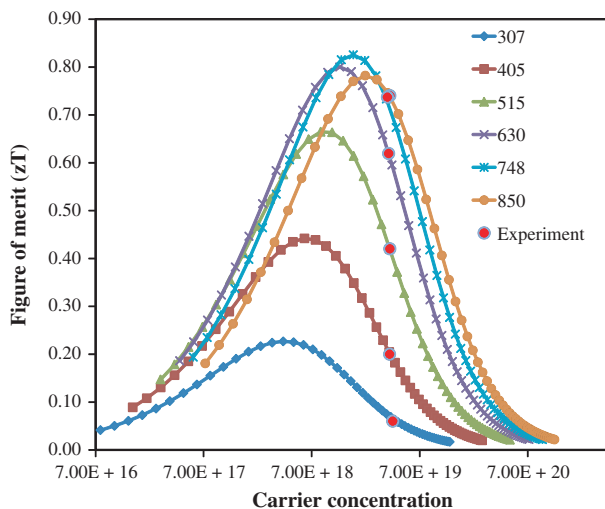


**Fig. 7.** Single parabolic band prediction of $zT$ values versus carrier concentration at different temperatures.

The SPB model prediction of $zT$ values versus carrier concentration using Eq. (9) at different temperatures are summarized in Figure 7.

$$zT = \frac{S^2}{L + (\psi\beta)^{-1}} \qquad (9)$$

The model predicts the maximum $zT$ value at 750 K at approximately $2 \times 10^{19}$ for the PbTe$_{0.62}$S$_{0.38}$ composite.

## 4. CONCLUSION

The thermoelectric transport properties of $n$-type PbTe$_{0.38}$S$_{0.62}$ alloy (critical composition) were investigated in the 300 k to 850 K temperature range. The maximum figure of merit of 0.75 was achieved at 800 K. The Single Parabolic Band model was employed to estimate the optimum Figure of merit for the $n$-type spinodally decomposed compound.

We have shown that the lattice thermal conductivity of the alloy is reduced by phonon scattering at interfaces and also disorder rising from solute atoms in solid solution phases that are in equilibrium at the temperature of interest. Scattering in solid solution resulting in an increase of the electrical resistivity was also observed. Therefore, there is a compromise between low thermal conductivity and high electrical conductivity in the spinodally decomposed alloys. It is also demonstrated that discontinuous coarsening occurs in the alloy during measurements. Our findings highlight the importance for careful analysis of multiple phase alloy thermoelectric materials and in particular alloys with small spacing between secondary phases that provides low diffusion distance to solute elements, in the prolonged performance of end generators.

## References and Notes

1. E. M. Levin, B. A. Cook, J. L. Harringa, S. L. Bud'ko, R. Venkatasubramanian, and K. Schmidt-Rohr, *Adv. Funct. Mater.* 21, 441 (**2011**).
2. L. E. Bell, *Science* 321, 1457 (**2008**).
3. Y. Zhao, J. S. Dyck, B. M. Hernandez, and C. Burda, *J. Am. Chem. Soc.* 132, 4982 (**2010**).
4. T. Wang, R. Mehta, C. Karthik, P. G. Ganesan, B. Singh, W. Jiang, N. Ravishankar, T. Borca-Tasciuc, and G. Ramanath, *J. Phys. Chem. C* 114, 1796 (**2010**).
5. X. Shi, J. Yang, S. Bai, J. Yang, H. Wang, M. Chi, J. R. Salvador, W. Zhang, L. Chen, and W. Wong-Ng, *Adv. Funct. Mater.* 20, 755 (**2010**).
6. X. Shi, J. Yang, J. R. Salvador, M. Chi, J. Y. Cho, H. Wang, S. Bai, J. Yang, W. Zhang, and L. Chen, *J. Am. Chem. Soc.* 133, 7837 (**2011**).
7. Y. Pei, X. Shi, A. LaLonde, H. Wang, L. Chen, and G. J. Snyder, *Nature* 473, 66 (**2011**).

8. J. P. Heremans, V. Jovovic, E. S. Toberer, A. Saramat, K. Kurosaki, A. Charoenphakdee, S. Yamanaka, and G. J. Snyder, *Science* 321, 554 (**2008**).

9. K. Biswas, J. He, Q. Zhang, G. Wang, C. Uher, V. P. Dravid, and M. G. Kanatzidis, *Nature Chem.* 3, 160 (**2011**).

10. E. S. Božin, C. D. Malliakas, P. Souvatzis, T. Proffen, N. A. Spaldin, M. G. Kanatzidis, and S. J. L. Billinge, *Science* 330, 1660 (**2010**).

11. Y. Pei, J. Lensch-Falk, E. S. Toberer, D. L. Medlin, and G. J. Snyder, *Adv. Funct. Mater.* 21, 241 (**2011**).

12. Y. Pei, N. A. Heinz, A. LaLonde, and G. J. Snyder, *Energ. Environmen. Sci.* 4, 3640 (**2011**).

13. J. Androulakis, Y. Lee, I. Todorov, D.-Y. Chung, and M. Kanatzidis, *Phys. Rev. B* 83, 195209 (**2011**).

14. S. Johnsen, J. He, J. Androulakis, V. P. Dravid, I. Todorov, D. Y. Chung, and M. G. Kanatzidis, *J. Am. Chem. Soc.* 133, 3460 (**2011**).

15. J. Q. He, J. R. Sootsman, L. Q. Xu, S. N. Girard, J. C. Zheng, M. G. Kanatzidis, and V. P. Dravid, *J. Am. Chem. Soc.* 133, 8786 (**2011**).

16. J. Androulakis, I. Todorov, J. He, D.-Y. Chung, V. Dravid, and M. Kanatzidis, *J. Am. Chem. Soc.* 133, 10920 (**2011**).

17. J. He, S. N. Girard, M. G. Kanatzidis, and V. P. Dravid, *Adv. Funct. Mater.* 20, 764 (**2010**).

18. L.-D. Zhao, J. He, C.-I. Wu, T. P. Hogan, X. Zhou, C. Uher, V. P. Dravid, and M. G. Kanatzidis, *J. Am. Chem. Soc.* 134, 7902 (**2012**).

19. H. Wang, Y. Pei, A. D. LaLonde, and G. J. Snyder, *Adv. Mater.* 23, 1366 (**2011**).

20. S. Gorsse, P. Bauer Pereira, R. Decourt, and E. Sellier, *Chem. Mater.* 22, 988 (**2009**).

21. T. Ikeda, L. A. Collins, V. A. Ravi, F. S. Gascoin, S. M. Haile, and G. J. Snyder, *Chem. Mater.* 19, 763 (**2007**).

22. T. Ikeda, V. A. Ravi, and J. Snyder, *J. Mater. Res.* 23, 2538 (**2008**).

23. S. N. Girard, J. He, X. Zhou, D. P. Shoemaker, C. M. Jaworski, C. Uher, V. P. Dravid, J. P. Heremans, and M. G. Kanatzidis, *J. Am. Chem. Soc.* 133, 16588 (**2011**).

24. S. Gorsse, P. Bellanger, Y. Brechet, E. Sellier, A. Umarji, U. Ail, and R. Decourt, *Acta Mater.* 59, 7425 (**2011**).

25. A. Volykhov, L. Yashina, and V. Shtanov, *Inorg. Mater.* 42, 596 (**2006**).

26. A. F. May, E. S. Toberer, A. Saramat, and G. J. Snyder, *Phys. Rev. B* 80, 125205 (**2009**).

27. A. D. LaLonde, Y. Pei, and G. J. Snyder, *Energ. Environmen. Sci.* 4, 2090 (**2011**).

28. M. F. Ashby and Y. J. M. Bréchet, *Acta Mater.* 51, 5801 (**2003**).

ARTICLE